

11A.4 MOBILE DOPPLER RADAR OBSERVATIONS OF A FRONT DURING IHOP

PAUL MARKOWSKI*

Department of Meteorology, Pennsylvania State University, University Park, PA

1. Introduction

Four mobile, truck-borne Doppler radars collected data along a front on 3 June 2002 during a convection initiation intercept of the International H₂O Project (IHOP). The dataset spans nearly seven continuous hours from roughly 1600–2300 UTC, affording the opportunity for a detailed study of the relationships between the kinematic and thermodynamic characteristics of the front. Convection failed to be initiated along the front, which was observed initially as a slowly moving cold front (Fig. 1), then as a stationary front, and finally as a warm front. This paper discusses some of the interesting observations made during the first deployment (Fig. 2), which approximately comprised the 1600–1830 UTC period.

2. Data and analysis methods

Three of the mobile radars [Doppler On Wheels (DOWs)] were similar to that described by Wurman et al. (1997). These radars operated with a wavelength of 3 cm; the stationary beamwidth, range gate spacing, and Nyquist velocity were 0.95°, 75 m, and 16.0 m s⁻¹, respectively. The fourth mobile radar [Shared Mobile Atmospheric Research and Teaching (SMART) radar] has been described

*Corresponding author address: Dr. Paul Markowski, Department of Meteorology, Pennsylvania State University, 503 Walker Building, University Park, PA 16802; e-mail: pmarkowski@psu.edu.

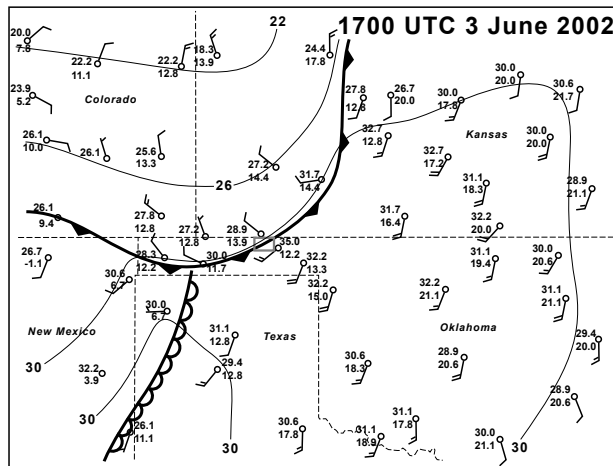


FIG. 1. Subjective surface analysis at 1700 UTC 3 June 2002, using conventional symbology to depict boundary locations. Station models show wind barbs in knots, and temperature and dew point in °C. Isotherms are drawn at 4°C intervals. The gray rectangular region outlined in the Oklahoma Panhandle represents the region depicted in Fig. 2.

by Biggerstaff and Guynes (2000). The radar operated with a wavelength of 5 cm; the stationary beamwidth, range gate spacing, and Nyquist velocity were 1.5°, 67 m, and 14.6 m s⁻¹, respectively.

Radial velocity data were edited to remove errors caused by low signal-to-noise ratio, second-trip echoes, sidelobes, ground clutter, and velocity aliasing. The correct pointing angles were obtained by comparisons of the ground clutter patterns to the known positions of landmarks visible in the clutter patterns. Pointing angles also were obtained from solar calibrations (Arnott et al. 2003) at some of the analysis times.

Radial velocity data were interpolated to a Cartesian grid having a horizontal and vertical grid spacing of 100 m. The lowest grid level was 100 m above the mean elevation of the radars. The interpolation was accomplished by way of a Barnes objective analysis using a smoothing parameter, κ , of 0.08 km². This choice of smoothing parameter yields a 70% response for features having a wavelength of 1.5 km, which is approximately 4 times the data spacing at a range of 25 km from the radars. At any grid point in the analysis region, this data spacing represents the coarsest resolution of the radars contributing to the wind synthesis (i.e., it is the resolution of the radar positioned farthest from the analysis grid point).

The three-dimensional wind synthesis was completed using the overdetermined dual-Doppler approach and the anelastic mass continuity equation (integrated upward), rather than a direct triple- or quadruple-Doppler solution. The former approach has some advantages over the latter

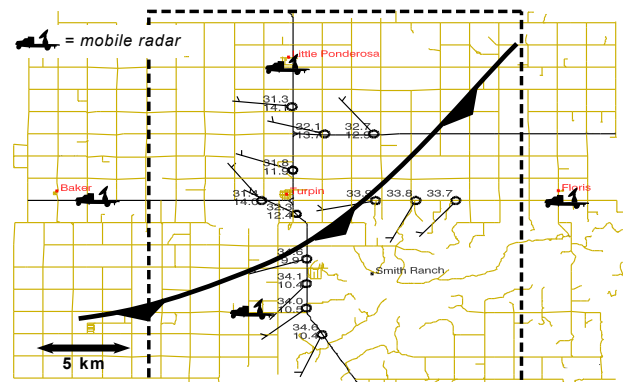


FIG. 2. Enlarged view of the domain in which the multiple Doppler wind synthesis was performed. The square region indicated with the dashed line represents the domain shown in Figs. 4–6. The station models indicate a few mobile mesonet observations obtained between 1658–1702 UTC, using the same symbology as in Fig. 1. The locations of the four mobile radars also are shown, as is the road network. North is at the top.

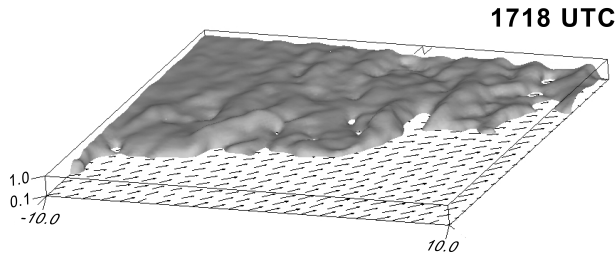


FIG. 3. Isosurface of $v = 2.0 \text{ m s}^{-1}$ at 1718 UTC, which roughly depicts the frontal surface. Horizontal wind vectors at 100 m also are shown. Units on the axes are km.

approaches, as demonstrated by Kessinger et al. (1987). The time resolution of the analyses is approximately 90 s, over which time synchronized scans were completed by three of the four radars. The fourth (SMART) radar completed a volume scan every 180 s.

3. Summary of observations

Perhaps the most noteworthy observation was that the structure of the front was considerably more complex than the conceptual models commonly presented in synoptic meteorology textbooks. This may not be surprising, given the unprecedented spatial and temporal resolution of the four-dimensional wind field afforded by the mobile radar network used herein. The frontal surface was hardly a smooth, gently sloping surface (Fig. 3). The front continually displayed kinks and wavelike structures, examples of which can be seen in the horizontal convergence, vertical velocity, and vertical vorticity fields shown in Figs. 4–6. It is well-known that interactions between fronts and rugged terrain can spawn some of the complex structures observed; however, these observations were made in a region of very little ($<50 \text{ m}$) topographic relief.

Maximum horizontal convergence and vertical vorticity values were $O(10^{-2}) \text{ s}^{-1}$, and maximum vertical velocities along the front exceeded 3 m s^{-1} at altitudes of 500–1000 m. One might suspect that the analyses displayed in Figs. 4–6 contain an excessive amount of spurious noise, possibly artifacts from the objective analysis, based on the numerous maxima and minima. It will be shown in the oral presentation by way of animations that these finescale details have vertical and temporal continuity. Though there is some artificial coupling in the vertical introduced by the objective analysis, there is no artificial coupling of fields in time. Each analysis is independent of prior and ensuing analyses. Thus, there is considerable confidence in the robustness of the fields shown. As might be expected, air parcel trajectories were a bit more “orderly” than the instantaneous velocity fields (Fig. 7).

Although the maximum values of horizontal convergence and vertical velocity generally were observed along the front, the horizontal convergence and vertical velocity fields also reveal structures away from the front that were associated with boundary layer convective cells (Figs. 4 and 5). The vertical velocities in the strongest cells approached 3 m s^{-1} , which were on the warm (south) side of the front.

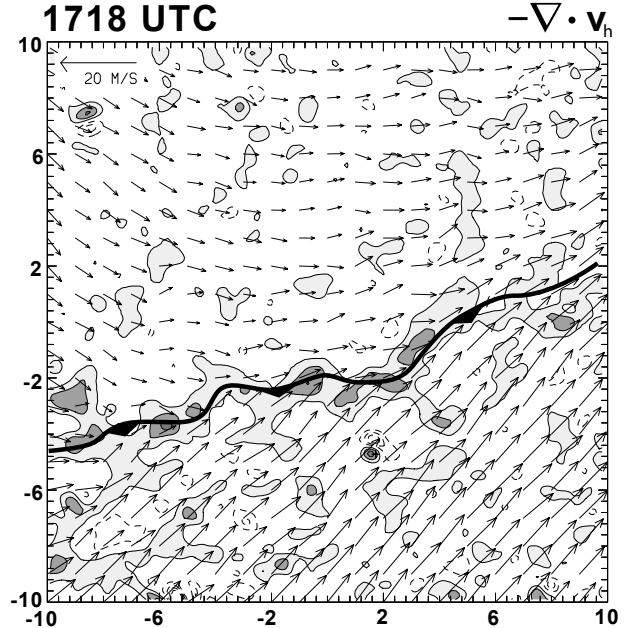


FIG. 4. Horizontal convergence, $-\nabla \cdot \mathbf{v}_h$, at 1718 UTC 3 June 2002 at an altitude of 100 m. Positive (negative) contours are solid (dashed) and are contoured at $2.5 \times 10^{-3} \text{ s}^{-1}$ intervals, beginning at $1.5 \times 10^{-3} \text{ s}^{-1}$ ($-1.5 \times 10^{-3} \text{ s}^{-1}$). Shaded regions indicate where horizontal convergence exceeds $1.5 \times 10^{-3} \text{ s}^{-1}$. Units on the axes are km.

It may be noteworthy that the correlation between vertical velocity and vertical vorticity was small within the domain (<0.15 at all levels and at all analysis times during the first deployment). In a large-eddy simulation of a convective boundary layer devoid of mesoscale boundaries, Kanak et al. (2000) found that local vertical velocity maxima tended to arise where vertical vortices also arose. Furthermore, several IHOP investigators have hypothesized that vortices developing along mesoscale boundaries may play important roles in convection initiation. The lack of a large correlation between vertical velocity and vertical vorticity may not refute such hypotheses, but the small correlations may be a manifestation of vortex dynamics that are more complicated than previously considered. Moreover, the small correlation also may not be surprising in consideration of the fact that $\partial\zeta/\partial t$, not ζ , is governed by $\partial w/\partial z$, not w .

4. Future work

The primary challenge of the future work will be combining thermodynamic information, particularly water vapor data, with the four-dimensional wind analyses obtained thusfar. It is anticipated that some of these analyses will be shown in the oral presentation, in addition to results from other deployments on 3 June. Buoyancy fields will be obtained by dynamic retrievals, and a wealth of remote and in situ water vapor measurements will be used to provide a more complete picture of the relationships between vertical motion and water vapor mixing ratio and virtual potential temperature—relationships that likely exert a large influence on convection initiation or its preclusion, as in this case.

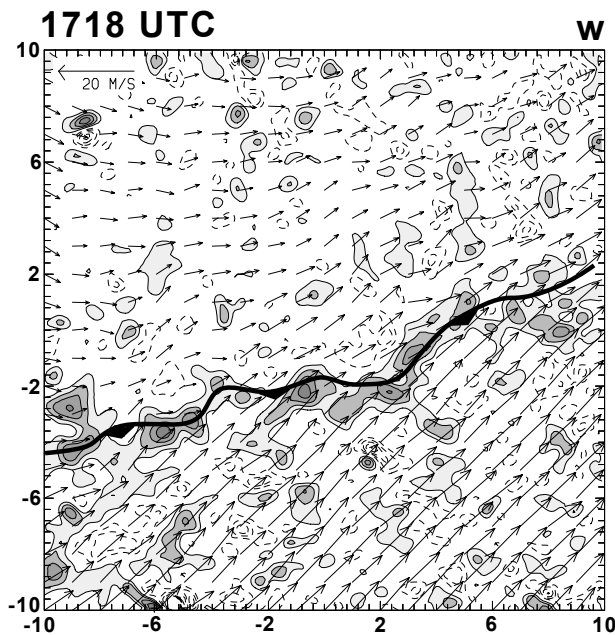


FIG. 5. As in Fig. 4, but for vertical velocity, w , at an altitude of 500 m. Positive (negative) contours are solid (dashed) and are contoured at 0.5 m s^{-1} intervals, beginning at 0.5 m s^{-1} (-0.5 m s^{-1}). Shaded regions indicate where vertical velocity exceeds 0.5 m s^{-1} .

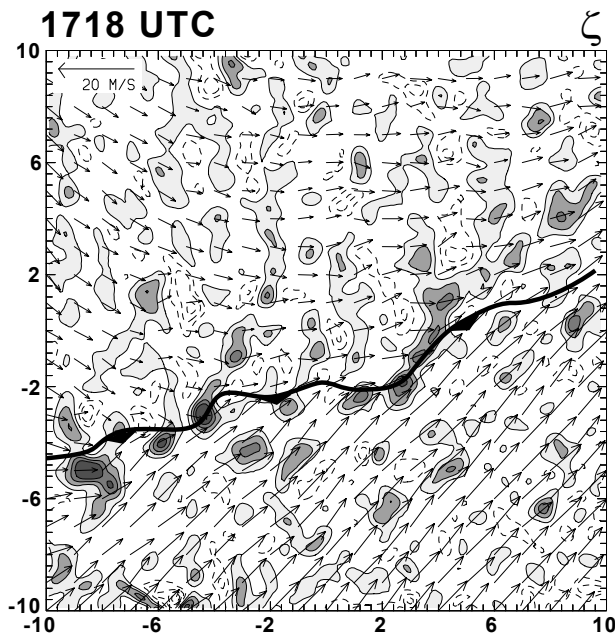


FIG. 6. As in Fig. 4, but for vertical vorticity, ζ , at an altitude of 100 m. Positive (negative) contours are solid (dashed) and are contoured at $2.5 \times 10^{-3} \text{ s}^{-1}$ intervals, beginning at $1.5 \times 10^{-3} \text{ s}^{-1}$ ($-1.5 \times 10^{-3} \text{ s}^{-1}$). Shaded regions indicate where vertical vorticity exceeds $1.5 \times 10^{-3} \text{ s}^{-1}$.

Baroclinity changes along the front also will be assessed as a function of time, and the kinematic changes associated with those baroclinity changes. Of particular interest will be the changes occurring between the times that the front transitioned from a cold front to a stationary front, and later to a warm front.

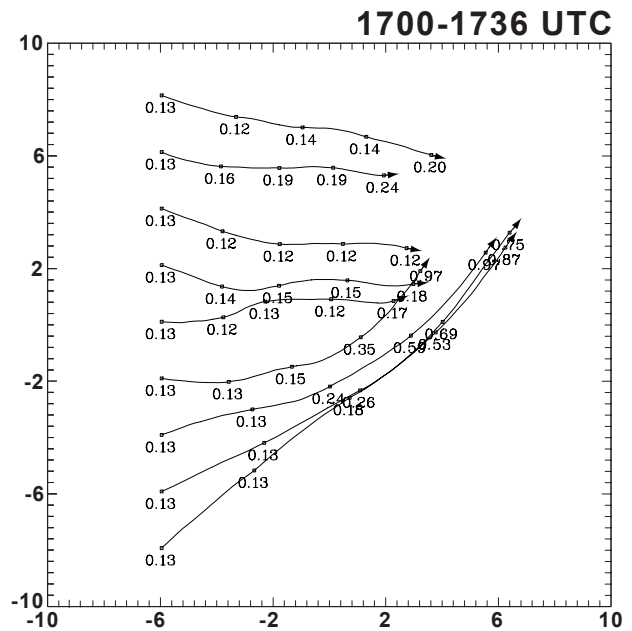


FIG. 7. An assortment of trajectories, beginning at 1700 UTC and terminating at 1736 UTC. Numerals along each trajectory indicate the height of the trajectory above the ground in km, at 9 min intervals.

Acknowledgments. I wish to thank Drs. Conrad Ziegler, Erik Rasmussen, Yvette Richardson, and Josh Wurman, with whom I have had a number of fruitful discussions. I also am grateful to Curtis Alexander, Christina Hannon, Nettie Arnott, and Mike Buban, who provided support in obtaining and editing radar data. Lastly, this work would not have been possible without the countless, tireless hours of data collection by the IHOP volunteers (too numerous to mention). Objective analyses of radial velocity data were performed using the NCAR REORDER software. Wind syntheses were performed using the NCAR CEDRIC software. Software designed by Erik Rasmussen also was used for some of the data editing and display tasks.

REFERENCES

- Arnott, N., Y. Richardson, J. Wurman, and J. Lutz, A solar calibration technique for determining mobile radar pointing angles. Preprints, *31st International Conf. on Radar Meteorology*. Seattle, Amer. Meteor. Soc., this volume.
- Biggerstaff, M. I., and J. Guynes, 2000: A new tool for atmospheric research. Preprints, *20th Conf. on Severe Local Storms*. Orlando, Amer. Meteor. Soc., 277–280.
- Kanak, K. M., D. K. Lilly, and J. T. Snow, 2000: The formation of vertical vortices in the convective boundary layer. *Quart. J. Royal Meteor. Soc.*, **126**, 2789–2810.
- Kessinger, C. J., P. S. Ray, and C. E. Hane, 1987: The Oklahoma squall line of 19 May 1977. Part I: A multiple Doppler analysis of convective and stratiform structure. *J. Atmos. Sci.*, **44**, 2840–2864.
- Wurman, J., J. Straka, E. Rasmussen, M. Randall, and A. Zahrai, 1997: Design and deployment of a portable, pencil-beam, pulsed, 3-cm Doppler radar. *J. Atmos. Oceanic Technol.*, **14**, 1502–1512.